Biosensors and Bioelectronics 54 (2014) 175–180

Contents lists available at ScienceDirect

Biosensors and Bioelectronics

journal homepage: www.elsevier.com/locate/bios

# High performance multi-spectral interrogation for surface plasmon resonance imaging sensors

A. Sereda [a,b,*], J. Moreau [a], M. Canva [a], E. Maillart [b]

[a] Laboratoire Charles Fabry, Institut d'Optique Graduate School, University Paris Sud, CNRS, 2 avenue Augustin Fresnel, 91127 Palaiseau Cedex, France
[b] Horiba Scientific, Avenue de la Vauve, Passage Jobin Yvon, CS 45002-91120 Palaiseau, France

ARTICLE INFO

*Article history:*
Received 17 July 2013
Received in revised form
20 September 2013
Accepted 23 October 2013
Available online 8 November 2013

*Keywords:*
Surface plasmon resonance
Biosensor
Multi-spectral imaging
DNA
Real-time measurement
Data dispersion

ABSTRACT

Surface plasmon resonance (SPR) sensing has proven to be a valuable tool in the field of surface interactions characterization, especially for biomedical applications where label-free techniques are of particular interest. In order to approach the theoretical resolution limit, most SPR-based systems have turned to either angular or spectral interrogation modes, which both offer very accurate real-time measurements, but at the expense of the 2-dimensional imaging capability, therefore decreasing the data throughput. In this article, we show numerically and experimentally how to combine the multi-spectral interrogation technique with 2D-imaging, while finding an optimum in terms of resolution, accuracy, acquisition speed and reduction in data dispersion with respect to the classical reflectivity interrogation mode. This multi-spectral interrogation methodology is based on a robust five parameter fitting of the spectral reflectivity curve which enables monitoring of the reflectivity spectral shift with a resolution of the order of ten picometers, and using only five wavelength measurements per point. In fine, such multi-spectral based plasmonic imaging system allows biomolecular interaction monitoring in a linear regime independently of variations of buffer optical index, which is illustrated on a DNA–DNA model case.



## 1. Introduction

Surface plasmon resonance (SPR) sensing is a well-established technique in the field of surface interactions characterization. Combining label-free and real-time capabilities, SPR-based systems are of particular interest for biomedical applications requiring high-throughput screening, since they allow the monitoring of multiple biomolecular interactions in parallel on a 2D bio-array format (Homola, 2008; Scarano et al., 2010).

In order to perform real-time measurements on such substrates, SPR systems classically operate in a so-called reflectivity interrogation mode (RIM), which requires a fixed wavelength and angle of incidence both chosen so to be close to the optimum sensitivity for the probe-target binding interaction studied. More precisely, the optimum working point ($\lambda_0$, $\theta_0$) depends on the local refractive index above the metallic layer which in turn is specific both to each biomolecular receptor immobilized at a given concentration on a given surface chemistry layer of the biochip and to the chosen running buffer. In practice, since several interactions are to be monitored simultaneously (Krishnamoorthy et al., 2010), the choice of a unique operating point does not provide a homogeneous and optimal response over the entire surface analyzed. This will lead to some significant data dispersion and limits the use of RIM especially when different families of probes are spotted on the same biochip. Moreover, for important buffer step index changes, the response in the RIM is no longer linear which limits the dynamic of detection.

These limitations can be overcome by performing either a wavelength or an angular interrogation on the sample, which both provide accurate measurements through the monitoring of the plasmon dip shift (Bardin et al., 2009; Beusink et al., 2008; Dostálek et al., 2007; Slavík and Homola, 2007). For both techniques, the sensitivity is mostly independent of the sample or the injected target solutions, and limited mainly by the experimental setup performances as well as by the data analysis used to determine the plasmon resonance dip shift. To achieve a good precision on the determination of the plasmon dip position, several measurements at different working points are required to acquire sufficient data on the angular or spectral resonance profile. In the case of the wavelength interrogation mode (WIM), the spectral profile of the resonance can be obtained either by a scan of the incident wavelength (Otsuki and Ishikawa, 2010) or the use of a spectrometer as the detector (Bardin et al., 2009; Bolduc et al., 2009; Slavík and Homola, 2007; Sutapun et al., 2011). While the former configuration allows maintaining a 2D imaging capability at the expense of the measurement rate, the latter provides instantaneous spectral information, but for a limited portion of the biochip (1D-arrays). Therefore, combining wavelength interrogation mode with an imaging system allowing high data throughput is still a challenge. Although systems operating in the angular interrogation mode

* Corresponding author.
*E-mail address:* alexandra.sereda@institutoptique.fr (A. Sereda).

0956-5663/$ - see front matter © 2013 Elsevier B.V. All rights reserved.
http://dx.doi.org/10.1016/j.bios.2013.10.049

(AIM) and covering this issue are currently available on the market (Beusink et al., 2008), their counterpart in the WIM has not been investigated extensively in the literature. In this contribution we present a detailed analysis of SPR multi-spectral imaging performances, both numerically and experimentally, with the aim of combining in wavelength interrogation mode both real-time and 2D imaging capabilities. We demonstrate that this technique can indeed provide a resolution equivalent to some of the best SPR imaging (SPRI) systems, but with a significant reduction in data dispersion and accurate measurements over a wider range of experimental conditions compare to the classical reflectivity interrogation mode.

## 2. Materials and methods

### 2.1. Experimental setup

The layout of the SPR imaging system is depicted Fig. 1. It is based on a spectral scanning modality, similar to a previously reported setup applied to the characterization of nanostructured gold surfaces (Nakkach et al., 2010). In the implementation presented in this article, wavelength interrogation can be performed from 500 nm to 850 nm using a white-light source (halogen lamp) coupled to a motorized monochromator (iHR 320, HORIBA Scientific). Careful consideration should be given to spatial and temporal coherence of the source, as it can strongly reduce the resolution and precision of SPRI systems. To this end, we have chosen the spectral FWHM to be equal to 13 nm and light is collected from the monochromator with a multimode fiber in order to minimize speckle. The beam is collimated at the output of the fiber with an angular divergence of 0.23° (internal angle after refraction in the prism). A motorized polarizer allows TM or TE polarization of the incident beam. Coupling between the incident light and the surface plasmons is achieved using a SF10 prism in the Kretschmann configuration. The incident beam is reflected by the gold biochip area covered by a microfluidic cell (1 cm in diameter, 90 μm depth) and imaged on a CCD camera (Pixelfly QE, 1280 × 1024 pixels with a full well capacity of 18,000 $e^-$). Temperature of the flow cell and the biochip is controlled with a 0.01 °C precision. Angle of incidence can be fixed within a range from 50° to 70° (internal angle). All experiments shown below were done at an incident angle of 55.54°, to excite a plasmon in the near-infrared region where the camera has the highest sensitivity.

In wavelength interrogation mode, TM images of the biochip surface, at the different interrogation wavelengths, are acquired as a function of time. 4 images are acquired and averaged for each wavelength. A typical acquisition time of 2 s per wavelength is needed, mostly due to the movement of the monochromator grating and integration time of the camera. The whole acquisition sequence is controlled with a home-made Labview program.

### 2.2. Reagents

The ssDNA sequences were chosen to serve the clinical purpose of a Cystic Fibrosis molecular diagnosis (Hottin et al., 2012). Target and probe sequences are centered on the M470V polymorphism located at position 1540 in exon 10 of Cystic Fibrosis Transmembrane Regulator (CFTR) gene. Referred to as TaMT and PrMT (Target and Probe with Mutated type sequence), these oligonucleotides have the following sequences: 5′CTCCCATAATCACCATTAGAAGTGA3′ and B5′TTTTTTTTTGACCGGTATGCGTTCTAATGGTGATT3′, where 5′ and 3′ indicate the two respective ends of the ssDNA sequence, and B the attached biotin. In order to account for the inhomogeneity due to surface chemistry and spotting process, a second ssDNA target was used for the data correction protocol. This calibration target (referred to as TaCal), exhibits the following sequence: 5′CGCGCGCATACCGGTCAAAA3′. Oligonucleotides were purchased from Eurogentec.

Plasmonic biochip substrates used consisted of 2 mm SF10 glass covered by a 3 nm chrome adhesion layer and a 51 nm gold film.

A cysteamine-based chemistry was used to functionalize the biochips (Spadavecchia et al., 2009) as it offers good performances in terms of specificity, probe binding strength and regenerative capability. Biotin functionalized probes can then be strongly attached to the last layer of streptavidin. Biotinylated oligonucleotides probes were spotted at a concentration of 5 μM. Resulting spots have a typical diameter of 300 μm, with a center-to-center spot spacing of 350 μm in both dimensions. Matrices with 12 × 12

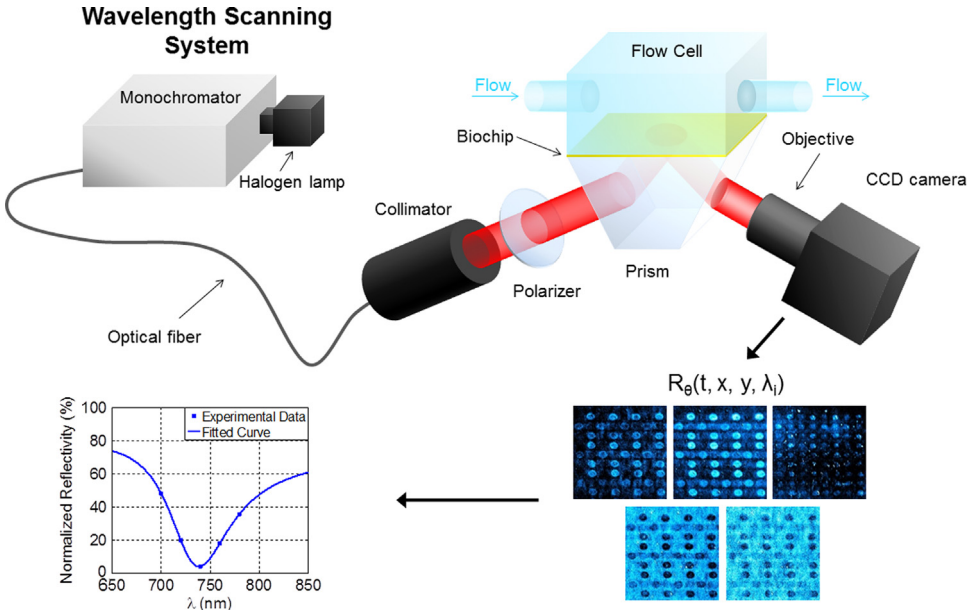


**Fig. 1.** SPR imaging setup, in a Kretschmann configuration. Light from a monochromator is collected in a multimode fiber, collimated and linearly polarized. After reflection on the biochip, consisting of a 51 nm gold layer deposited on a SF10 glass slide, the light beam is sent on a CCD camera. In wavelength interrogation mode, images at different wavelengths are acquired through time which allows the extraction of the plasmon dip shift on every point of the biochip's surface.

spots were prepared, with many replicates to obtained significant statistics. The transducing surfaces were then stored at +4 °C until used. All experiments were performed in PBS (Phosphate Buffered Saline, Sigma Aldrich) buffers at different concentrations, referred to as PBS 1×, PBS 3× and PBS 5× in the experimental section. When diluted to a 1× concentration, the solution contains a phosphate buffer at 10 mM and sodium chloride at 154 mM. Similarly, the molarities of the 3× and 5× buffers are respectively 30 mM and 50 mM for the phosphate buffer, and 0.462 M and 0.77 M for sodium chloride. The solutions pH values are 7.2, 6.9 and 6.7, respectively, for PBS 1×, PBS 3× and PBS 5× concentrated.

### 2.3. Analysis of the SPR signal

The WIM signal is defined as the evolution of the spectral position of the plasmon dip. Its determination relies not only on the performances of the experimental setup, but also on the use of an appropriate data processing. In this field, some studies rely on a polynomial fitting (Wang et al., 2011), the centroid method (Thirstrup and Zong, 2005) or the optimal linear data analysis (Chinowsky et al., 1999). In our case, where the number of interrogation wavelengths is relatively small, we found more accurate results using an asymmetric pseudo-Lorentz function with the following expression:

$$R(\lambda) = R_0 \times \left(1 - D\frac{W + A \times (\lambda - \lambda_0)}{W^2 + (\lambda - \lambda_0)^2}\right)$$

As for the five fitting parameters: $D$, $W$, $A$ and $\lambda_0$ refer respectively to the depth, width, asymmetry and position of the resonance profile, while $R_0$ relates to the source intensity (Tobiška and Homola, 2005). This expression, which is derived directly from the plasmon dispersion relation, as described in Kurihara et al. (2002), fits well the asymmetric shape of the reflectivity spectral profile. Based on this equation, a home-made Matlab program was developed to extract the plasmon dip shift $\Delta\lambda$ associated to each region of interest on the sample and calculate the statistics corresponding to each spectral interrogation configuration.

In order to directly compare the results obtained in WIM to the reflectivity variation signal used in classical SPRI systems, the reflectivity variations can also be computed on the fitted plasmon dip, at a virtual wavelength working point. Note that, because this working point is the same for all the different spots on the biochips and all experimental conditions found during the experiment, it can be chosen to be optimal in term of signal amplitude only for a given family of spots of interest in a given buffer, but will then be sub-optimal in any other case. To reduce any bias in the comparison between the two interrogation modes, the spectral interrogation wavelengths were carefully chosen to contain the reflectivity variation optimal working point, allowing both measurements to be performed at the same time.

## 3. Results

### 3.1. Determination of the optimal number of interrogation wavelengths

In WIM, the number of interrogation wavelengths has to be carefully chosen so as having an accurate monitoring of the plasmon dip shift, while not degrading too much the real-time capability of the system. To address this issue, the optimal configuration was investigated as follows. Experimentally, the spectral position of the plasmon dip was measured on a bare gold biochip in water, using the previously described fitting procedure. The standard deviation of this position over time is defined as the resolution of the WIM signal. In order to assess statistical significance, this signal was estimated on fifty 40 × 40 pixels, arbitrarily defined and supposedly identical, regions of interest on the biochip. This experiment was repeated with different numbers of interrogation wavelengths, from 5 to 13 with a fixed spectral step of 10 nm. All wavelengths were chosen symmetrically around the plasmon resonance wavelength, 740 nm. Fig. 2 shows the resolution of the WIM signal (spectral position of the plasmon dip $\lambda_{min}$) as a function of the number of interrogation wavelengths.

Numerical simulations, based on a plasmon spectral profile obtained with a previously reported extended Rouard method (Lecaruyer et al., 2006), were performed to confront experimental data. With the assumption of shot noise limited images, they predict an increase in resolution as a function of the inversed square root of the number of interrogation wavelengths. However, the thermal noise in the fluidic cell must also be accounted for since it directly impacts the refractive index of the aqueous medium above the biochip. When taken into consideration, this effect slightly lowers the predicted gain in resolution with the number of wavelengths. Furthermore, since only a small number of interrogation wavelengths can be realistically used in a fast imaging system, no significant improvement can be expected by using more than the minimum needed for the plasmon dip fit. Therefore, using adequate data processing, as low as five scanning wavelengths is enough to reach close to minimal data dispersion experimentally. We explain the difference between experimental results and simulation by the residual speckle noise in the images, which increases with the number of interrogation wavelengths and therefore the acquisition time chosen.

According to these results, we can estimate the resolution of our setup to be equal to 7 pm, which corresponds to a limit of detection in terms of step index of around $2.10^{-6}$ RIU. It is important to note that the same resolution is obtained from experiments performed on our setup in the RIM: the limit of detection is not affected by the interrogation mode and remains constrained by the noise properties of our setup. Moreover, this value is comparable to the precision previously reported in WIM or AIM imaging system (Beusink et al., 2008; Otsuki and Ishikawa, 2010). Spectrometer detector configurations (Bardin et al., 2009; Bolduc et al., 2009), which provide hundreds of data points on the resonance profile but at the expense of the imaging capability, achieve an order of magnitude better in resolution as expected from our shot noise limited calculations.

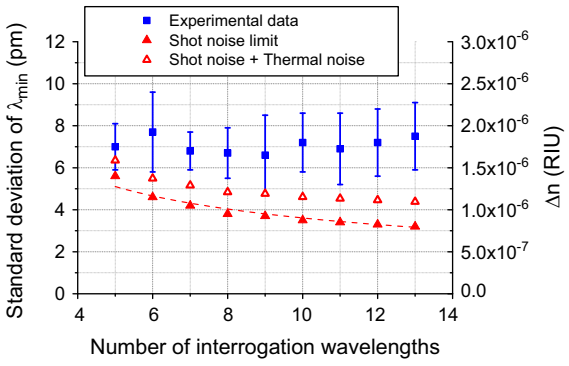


**Fig. 2.** Evolution of the standard deviation of the WIM signal as a function of the number of interrogation wavelengths. Right $y$-axis shows the corresponding minimum step-of-index resolution. The experimental data (square) was obtained on a bare gold biochip in water, monitored using a variable number of interrogation wavelengths, with a spectral step fixed at 10 nm. The error bar is related to the dispersion of the values of the different regions on the gold surface. Simulations are computed on the assumption of shot noise limited images, with (open triangle), and without (full triangle) a thermal noise of ±0.005 °C.

Another important question when choosing spectral interrogation configuration for an optimum WIM signal is the impact on the position of the wavelength comb compared to the plasmon resonance wavelength. Ideally, the center wavelength of the comb should be equal to the plasmon resonance wavelength. However, if large variation of this plasmon resonance wavelength is expected during the experiment, then the accuracy of the WIM signal could be seriously reduced due to a completely off-centered comb. Similarly, inhomogeneity of biochip's surface or difference in the nature of the immobilized biomolecular probes will also lead to different plasmon resonance wavelengths across the biochip. Fig. 3(a) shows the accuracy of the WIM signal, defined as the difference between the extracted spectral plasmon dip shift and its theoretical value, as a function of the relative position of the comb to the resonant wavelength. Results are shown in the case of 5 and 7 interrogation wavelengths and for spectral steps of 10 nm and 20 nm.

It appears that the accuracy is more or less constant and independent of the position of the comb for a certain range until a clear cutoff is seen. As expected, more scanning wavelengths allow a greater dynamic range in WIM signal. It appears also that using 10 nm steps gives more latitude on the positioning of the comb and therefore a better dynamic range (approximately 40 nm, which is equivalent to a step index range of $10^{-2}$ RIU). This result is further illustrated in Fig. 3(b) which shows the experimental responses of seventy regions of interest on a bare gold biochip, for different buffer step indexes ranging from $1.10^{-5}$ to $1.10^{-2}$, using a five interrogation wavelength implementation. The experimental plasmonic signal was simultaneously recorded using both reflectivity and spectral interrogation. In RIM, the limitation induced by the use of a single working point starts around an index step of $2.10^{-3}$, after which the signal recorded is no longer linear and highly dispersed. As expected from simulations, the dynamic range in WIM is significantly improved, up to a point where the plasmon curve is being shifted too far from the fixed position of the wavelength comb: the pseudo-Lorentz fit is no longer robust which leads to increased error on the determination of the plasmon dip position.

Finally, we can conclude from this study that the choice of the spectral interrogation configuration is mainly a compromise between the acquisition speed, limited by the number of scanning wavelengths, and the dynamic range needed for a given application. In the following experiments, we chose to work with five or seven interrogation wavelengths.

### 3.2. Comparison between WIM and RIM: Evaluation of the gain in data dispersion

Using a seven interrogation wavelength implementation, which provides accurate measurements up to $\pm 5.10^{-3}$ RIU buffer index variation range, we investigate the robustness of our method in terms of data dispersion compared to the classical RIM. As in the previous experiment, both RIM and WIM signals were recorded simultaneously for seventy regions of interest on a bare gold biochip. In order to avoid any bias due to the different dynamic ranges of the two methods, we injected buffer step indexes from $1.10^{-4}$ to $2.10^{-3}$. For each step of index and each interrogation method, the standard deviation was calculated over the seventy responses and divided by the average signal value, to obtain the relative dispersion represented in Fig. 4(a) below.

For small buffer index variations ($\Delta n \sim 10^{-4}$), the dispersion of the responses recorded using both RIM and WIM are identical. As the step indexes increase, the difference between the two techniques appears and is further amplified. The monitoring of the plasmon dip shift follows the buffer variations and provides constant dispersion, while the RIM signals exhibit larger dispersion over the investigated index range.

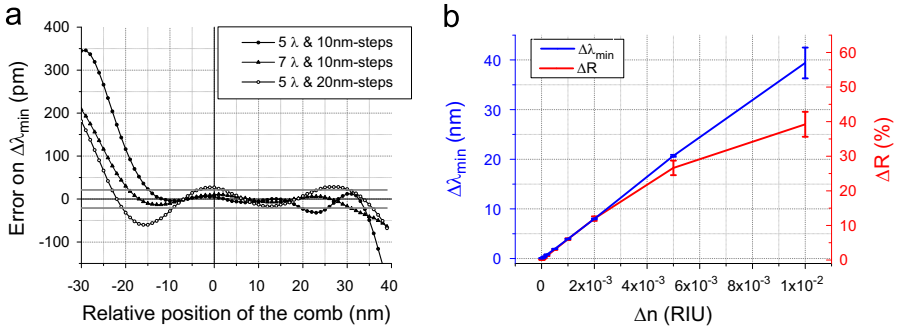


**Fig. 3.** (a) Simulation of the evolution of the measurement accuracy (error on the plasmon dip shift) as a function of the relative position between the center wavelength of comb and the plasmon resonance wavelength. The horizontal solid lines at $y = \pm 21$ correspond to the $\pm 3\sigma$ resolution limit. (b) Experimental comparison of dynamic ranges in RIM and a WIM configuration based on 5 wavelengths with 20 nm steps.

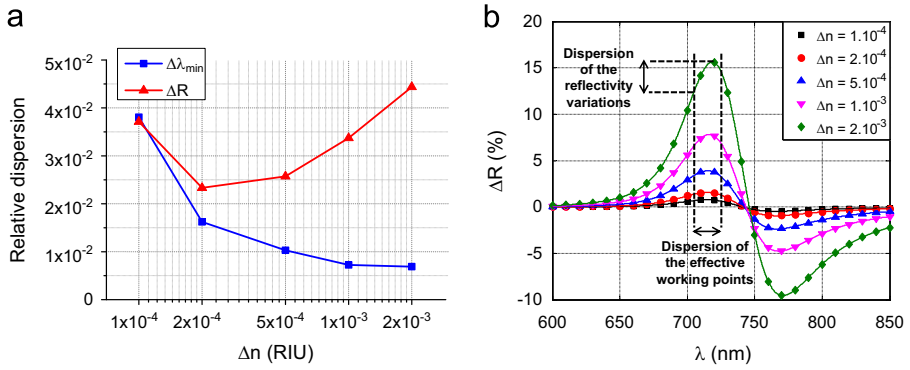


**Fig. 4.** (a) Comparison of experimental relative data dispersion in RIM and WIM for different buffer step indexes ranging from $1.10^{-4}$ to $2.10^{-3}$ on a bare gold biochip. (b) Simulations of the reflectivity difference spectra for the step indexes studied.

This behavior can be explained by looking at Fig. 4(b), which shows the plasmon responses of a perfectly homogeneous biochip, in terms of reflectivity variations, for the different step indexes investigated. However, because of the unavoidable surface inhomogeneity of the biochip, there is a dispersion of the plasmon responses, which is equivalent to considering that the reflectivity variations are in fact measured over a range of effective working points. The larger the step of index, the larger the dispersion in the RIM signals.

### 3.3. Application to DNA–DNA interaction monitoring; WIM vs. RIM signals

The comparison between WIM and RIM signals was further illustrated on the model case of DNA–DNA interaction monitoring. In particular, optimal conditions of the stringence of the buffer solution were investigated using both techniques. To this aim, the following experiment was performed on a cysteamine-based chemistry biochip described above: target ssDNA solution (TaMT) was first injected in PBS 1 ×, and removed by a regeneration step after 15 min. The running buffer was then changed to PBS 3 ×, and the target solution was injected, followed by regeneration. Finally, this experiment was repeated in PBS 5 ×. The concentration was chosen to be 0.1 μM for the TaMT sequence, for all of the three buffers. For all experiments, monitoring of the interactions between the targets and the probe molecules grafted on the gold biochip surface was performed using both RIM and WIM. For the RIM, the optimal working point was determined in the PBS 1 × buffer and kept constant during the experiment. Also, in order to compare strictly the performances of the two interrogation techniques, it is essential to account and cancel the data dispersion induced by the spot-to-spot reactivity differences. To this aim, a TaCal sequence was also injected after each buffer change to calibrate the DNA spot responses and correcting the following TaMT–PrMT interaction according to a previously reported self-calibration method (Hottin et al., 2012). The final kinetics of the interactions studied in the three buffers are presented in Fig. 5.

From WIM signals, DNA–DNA hybridization appears to be favored by the stringency of the buffer solution. This first observation is consistent with previous studies, which point to a reduction of electrostatic penalty when the buffer ionic strength is increased (Fuchs et al., 2010; Irving et al., 2010). However, the RIM data does not follow this rule and presents a lower reflectivity variation value than expected in the case of PBS 3 ×, and even shows a decrease in the signal in PBS 5 ×. In order to highlight this behavior, the normalized values of the hybridization signals after 15 min for RIM and WIM are shown in Fig. 6.

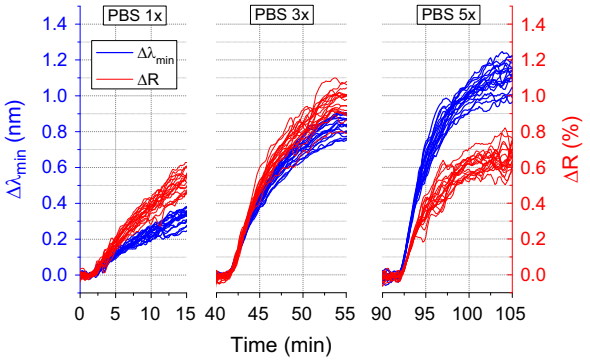


**Fig. 5.** TaWT–PrWT interaction kinetics in the PBS 1 ×, PBS 3 × and PBS 5 × buffers recorded using the RIM (in red) and the 5-wavelength interrogation technique (in blue). (For interpretation of the references to color in this figure legend, the reader is referred to the web version of this article.)

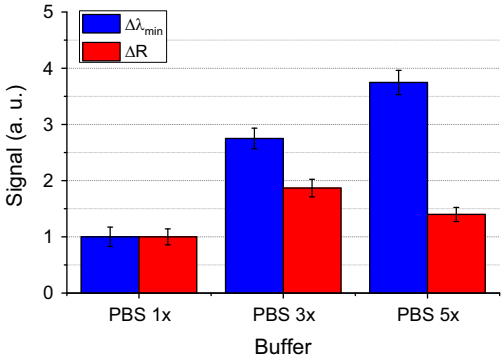


**Fig. 6.** Hybridization signals after 15 min for the TaMT–PrMT interaction recorded in the RIM (in red) and the 5-wavelength interrogation technique (in blue), in PBS 1 ×, 3 × and 5 × concentrated. The values obtained in PBS 1 × were used as a reference to normalize those recorded in the PBS 3 × and PBS 5 × buffers, for both of the interrogation techniques. (For interpretation of the references to color in this figure legend, the reader is referred to the web version of this article.)

The lower hybridization signals in the PBS 3 × and 5 × buffers is clearly due to the limited dynamic range of the RIM, as the plasmon curves are shifted too far from the initial optimal working point. On the other hand, the 5-wavelength interrogation technique proves to be more robust towards buffer index variations, as demonstrated in the previous section.

## 4. Conclusion

In the field of SPR sensing, several interrogation techniques have been developed to meet different measurement requirements. For instance, while the RIM allows a high data throughput and accurate measurements but within a limited buffer index variation range, the AIM and WIM offer extended dynamics and higher resolution at the expense of 2D imaging. In this contribution, we have shown how to optimize a WIM-based measurement that allows keeping both 2D imaging and real-time capabilities. With only five wavelengths and an asymmetric pseudo-Lorentz fitting function, the presented method exhibits a resolution of 7 pm on the plasmon dip position determination. This value corresponds to a limit of detection of $2.10^{-6}$ RIU in terms of index step and a minimum surface coverage detectable of around 1 pg $mm^{-2}$, which is equivalent to the resolution obtained in RIM experiments performed on our setup. Moreover, the performances, both in terms of resolution and accuracy, are constant within a dynamic range of $\pm 5.10^{-}3$ RIU of the surrounding media. This allows significant gain in data quality compared to the RIM, where the optimal conditions are strongly dependent on the buffer index variations and the surface chemistry inhomogeneity. This would be especially useful in multichannel fluidic experiments where analytes are simultaneously delivered onto the gold surface in different buffer conditions. Also, nanostructured gold film which usually exhibit broad plasmonic resonances leading to low RIM signals could take advantage of such an interrogation technique.

## Acknowledgements

The work presented in this paper is part of the PIRANEX project thematic (ANR-12-NANO-0016) and was also partially supported by the LUMAT Federation.

## References


Bardin, F., Bellemain, A., Roger, G., Canva, M., 2009. Biosens. Bioelectron. 24 (7), 2100–2105.
Beusink, J.B., Lokate, A.M.C., Besselink, G.A.J., Pruijn, G.J.M., Schasfoort, R.B.M., 2008. Biosens. Bioelectron. 23 (6), 839–844.
Bolduc, O.R., Live, L.S., Masson, J.-F., 2009. Talanta 77 (5), 1680–1687.
Chinowsky, T.M., Jung, L.S., Yee, S.S., 1999. Sens. Actuators, B 54 (1–2), 89–97.
Dostálek, J., Kasry, A., Knoll, W., 2007. Plasmonics 2 (3), 97–106.
Fuchs, J., Fiche, J.B., Buhot, A., Calemczuk, R., Livache, T., 2010. Biophys. J. 99 (6), 1886–1895.
Homola, J., 2008. Chem. Rev. 108 (2), 462–493.
Hottin, J., Moreau, J., Bellemain, A., Canva, M., 2012. Analyst 137 (13), 3119–3125.
Irving, D., Gong, P., Levicky, R., 2010. J. Phys. Chem. B 114 (22), 7631–7640.
Krishnamoorthy, G., Carlen, E.T., van den Berg, A., Schasfoort, R.B.M., 2010. Sens. Actuators, B 148 (2), 511–521.
Kurihara, K., Nakamura, K., Suzuki, K., 2002. Sens. Actuators, B 86 (1), 49–57.
Lecaruyer, P., Maillart, E., Canva, M., Rolland, J., 2006. Appl. Opt. 45 (33), 8419–8423.
Nakkach, M., Duval, A., Ea-Kim, B., Moreau, J., Canva, M., 2010. Opt. Lett. 35 (13), 2209–2211.
Otsuki, S., Ishikawa, M., 2010. Biosens. Bioelectron. 26 (1), 202–206.
Scarano, S., Mascini, M., Turner, A.P.F., Minunni, M., 2010. Biosens. Bioelectron. 25 (5), 957–966.
Slavík, R., Homola, J., 2007. Sens. Actuators, B 123 (1), 10–12.
Spadavecchia, J., Moreau, J., Hottin, J., Canva, M., 2009. Sens. Actuators, B 143 (1), 139–143.
Sutapun, B., Somboonkaew, A., Amrit, R., Houngkamhang, N., Srikhirin, T., 2011. Sens. Actuators, B 156 (1), 312–318.
Thirstrup, C., Zong, W., 2005. Sens. Actuators, B 106 (2), 796–802.
Tobiška, P., Homola, J., 2005. Sens. Actuators, B 107 (1), 162–169.
Wang, Z., Diamond, J.J., Hou, R., Wang, K., Song, L., Su, Y., Zheng, Z., Zhu, J., 2011. Sens. Actuators, B 151 (2), 309–319.